Chemical Engineering Science 215 (2020) 115385

Contents lists available at ScienceDirect

Chemical Engineering Science

journal homepage: www.elsevier.com/locate/ces

Isothermal drying of plant-based food material: An approach using 2D polydimethylsiloxane (PDMS) micromodels

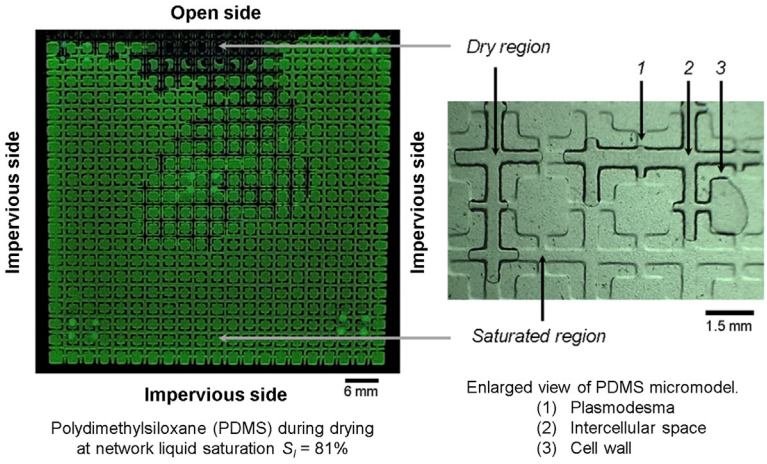
Marco Guzmán-Meza [a], João Borges Laurindo [b], Marcela Jarpa-Parra [c], Luis Segura-Ponce [a,*]

[a] Food Engineering Department, Universidad del Bío-Bío, P.O. Box 447, Chillán, Chile
[b] Department of Chemical and Food Engineering, Federal University of Santa Catarina, 88040-900 Florianópolis, SC, Brazil
[c] Universidad Adventista de Chile, Box 7-D, Chillán, Chile

HIGHLIGHTS

- Proposed new porous medium approach to represent plant-based food material.
- Developed methodology to build micromodels representing plant-based food material.
- Homogeneous depth of pores and throats obtained by the Toyobo-KM43GS plate.
- Pyranine aqueous solution allowed easy observation of drying fronts.

GRAPHICAL ABSTRACT



Polydimethylsiloxane (PDMS) during drying at network liquid saturation S_l = 81%

ARTICLE INFO

Article history:
Received 29 July 2019
Received in revised form 4 November 2019
Accepted 22 November 2019
Available online 26 November 2019

Keywords:
Porous media
Micromodels
PDMS
Plant-based food material
Drying mechanisms

ABSTRACT

The aims of this study were to build PDMS micromodels that simulated plant-based food material, and use them to investigate the drying mechanisms at pore-scale, the drying front morphologies and the drying curves during the isothermal drying process. Micromodels were built using a modified photolithographic technique. Three normal pore size distribution functions were developed to simulate the plasmodesma, intercellular space, and cell wall. Micromodels were impregnated with a pyranine aqueous solution and placed on a balance illuminated with ultraviolet light. Isothermal drying was developed by natural convection (20 °C). Drying front morphologies displayed a hierarchical behavior in which pores with the largest diameter dried first. Drainage and surface evaporation sequences and internal evaporation controlled the drying of PDMS micromodels. The micromodels were useful to simulate plant-based food material and study isothermal drying of such porous media. The results led to the proposal of some drying mechanisms that were involved.

© 2019 Elsevier Ltd. All rights reserved.

1. Introduction

Drying is a common method to remove liquid from a porous material by evaporation. In this process, the gas phase replaces

* Corresponding author.
E-mail address: lsegura@ubiobio.cl (L. Segura-Ponce).

https://doi.org/10.1016/j.ces.2019.115385
0009-2509/© 2019 Elsevier Ltd. All rights reserved.

the liquid phase present in the pore space as a result of liquid evaporation. Drying is a remarkable process in many industrial applications such as in ceramic, food, paper, and wood (Mujumdar, 2006). These materials are porous media at different scales. Wood and some food are plant tissues with complex structures where several drying mechanisms could be present at different stages of the process. Their relative importance depends on drying conditions, pore geometry, pore topology, and wall composition of the porous medium (Segura, 2007). The study of transport phenomena involved in drying a plant-based food material improves both the process and dried product quality. Currently, some plant-based food material drying studies have incorporated transmembrane transport coupled to a diffusive intercellular mechanism in a porous medium (Huang et al., 2012; Xiao et al., 2014) together with water transport by diffusion from a continuous medium approach (Fanta et al., 2014). Likewise, cell rupturing mechanisms and water migration from cells of plant-based food material during drying has been investigated. Khan et al. (2018a) emphasize that comprehension of the migration mechanisms of cellular water is key for accurate prediction of actual heat and mass transfer during drying of plant-based food material. Although considerable efforts have been made in this regard (Huang et al., 2012; Xiao et al., 2014; Fanta et al., 2014; Khan et al., 2017, 2018a, 2018b; and Rahman et al., 2018b), it is not clear the role of drying mechanisms in plant-based food material, since current techniques do not allow in-situ monitoring the cell water migration at pore level during drying process.

Micromodels are a good tool to investigate different phenomena that occurs during drying at pore scale, such as drying mechanisms, transport and crystallization of non-volatile compounds, drying patterns morphologies, and microstructural changes (Eloukabi, et al., 2011; Laurindo and Prat, 1996, 1998; Oyarzún and Segura, 2009; Sghaier and Prat, 2009; Shaw, 1986, 1987; Vorhauer et al., 2013). According to Oyarzún and Segura (2009), 2D transparent micromodels can be defined as networks of pores and constrictions that simulate the complexity of natural porous media. These microfluidic devices allow the visualization of complex interface solid/liquid/fluid interactions and their relations with the geometry and topology of the pore space during the drying process. Since the pioneering work of Daian and Saliba (1991), Nowicki et al. (1992), and Prat (1993), several researchers have used micromodels to study various processes involving porous media, for example, drying (Díaz et al., 2011; Eloukabi et al., 2011; Laurindo and Prat, 1996, 1998; Oyarzún and Segura, 2009; Segura et al., 2013, 2015; Sghaier and Prat, 2009; Vorhauer et al., 2013), freeze drying (Segura and Oyarzun, 2012), and vacuum impregnation (Badillo et al., 2011). There have also been studies of the frying process using glass micromodels (Cortés et al., 2014, 2015, 2016).

Some studies have built micromodels in order to reproduce plant tissues such as wood and food. Oyarzún and Segura (2009) built a glass micromodel that captures the pore-level anatomy of a longitudinal-tangential section of softwoods. Díaz et al. (2011) and Cortés et al. (2014, 2015, 2016) built rigid micromodels that used a monomodal porous medium approach to represent the plant tissue of carrots, potatoes, and apples. In the monomodal porous medium approach, large portions of solid material and a narrow network of interconnected pores and throats can be identified. But micromodels built using this approach do not completely represent the plant tissue microstructure, and the formed porous network only contains a small amount of liquid (Huang et al., 2012; Xiao et al., 2014). It is known that a large amount of the moisture content (80% to 95%) of plant-based food material is enclosed inside the cell (Halder et al., 2011; Khan et al., 2016). As the monomodal porous medium approach not includes the intracellular space and only contains a small amount of liquid, this approach not allows to represent the plant-based food material. The research group lead by PhD Segura has developed methods to produce transparent micromodels of glass (Oyarzun and Segura, 2009), polyester resin (Díaz et al., 2011), and polydimethylsiloxane (PDMS) (Segura et al., 2013, 2015). However, practically all the micromodels built by PhD Segurás research group have been based on the monomodal approach. Consequently, it is necessary to build micromodels that represent plant-based food material architecture and use them to develop drying experiments to understand the drying mechanisms involved in this type of food. It is worth to mention that the knowledge about the drying mechanism at pore-scale is an important input to develop more realistic mathematical models to describe drying process (Oyarzún and Segura, 2009).

To complete these tasks, a great deal of statistical information about the plant-based food material is needed. Plant tissue is comprised of various structures that are classified according to their size in three main scales. The cell wall arrangements and membranes constituted the mesoscale. The microscale consists of individual cells with their spaces and organelles. The nanoscale is mainly comprised of cellulose fibers and plasmodesmata (Jeffery et al., 2012). Numerous authors have characterized some cellular components of fruits and vegetables (Hallett et al., 1992; Joardder et al., 2015; Roy et al., 1997; Sutherland et al., 1999); unfortunately, established size distributions for plasmodesmata and cell walls have not yet been provided. On the other hand, there is information regarding cell size and intercellular spaces. Pieczywek and Zdunek (2012) studied the microstructure of two apple varieties (*Golden Delicious* and *Champion*) using confocal scanning laser microscopy. These authors found that the intercellular spaces (pores) of both apple varieties were greater than the cells in terms of area and perimeter. Herremans et al. (2015) used X-ray micro-CT to analyze the 3D microstructure of the three apple varities *Braeburn*, *Kanzi*, and *Jonagold*. These authors used a normal distribution function ($p > 0.05$) to model cell size and intercellular spaces of the three apple varieties. Recently, Rahman et al. (2018a) found comparable results in a drying study with *Granny Smith* apples. The authors characterized the apple microstructure by X-ray microtomography and obtained similar equivalent diameters for the intra- and intercellular spaces. Summarizing, there is enough statistical information to build micromodels that represent plant-based food material, and the normal pore size distributions functions are the key in order to complete these task.

The main objectives of this work were to build PDMS micromodels that simulated plant-based food material, and use them to investigate the drying mechanisms at pore-scale, the drying front morphologies and the drying curves during the isothermal drying process. The paper is organized as follows. The new pattern of porous medium developed in this research study is shown in Section 2. Section 3 deals with the PDMS micromodel fabrication procedure, the description of the isothermal drying experiments and statistical analysis. The results are in Section 4 and include PDMS micromodel appearance, kinetic, and drying rate curves, drying front morphologies and the possible drying mechanisms involved during the drying of PDMS micromodels. Finally, conclusions are summarized in Section 5.

2. Development of new pattern of porous medium

A new porous medium approach was developed to obtain micromodels that could simulate plant-based food material. Fig. 1 shows the three types of porous media monomodal, bimodal, and modified bimodal. The monomodal porous medium displayed in Fig. 1a consists of four throats and a pore body (node) formed at the connection of the four throats. The monomodal porous med-

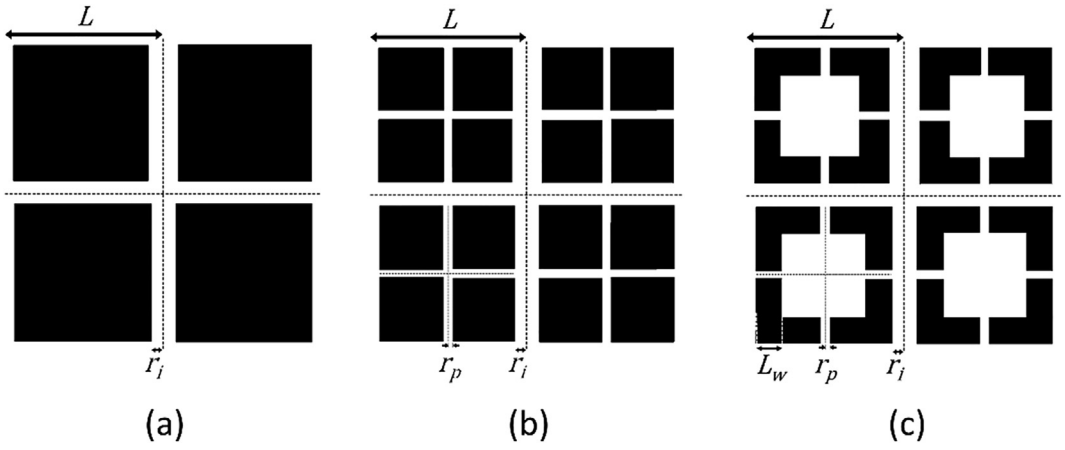


Fig. 1. Diagrams show different types of porous media: (a) monomodal, (b) bimodal, and (c) modified bimodal.

ium is defined by the two characteristic parameters of pore-body-center to pore-body-center distance (L) and throat radius (r_i) (Laurindo and Prat, 1996, 1998; Prat, 1993). The bimodal porous medium illustrated in Fig. 1b consists of four main throats, a main pore body (node), sixteen secondary throats, and four secondary pore bodies formed at the connection of the secondary throats. The bimodal porous medium is further defined by a third characteristic parameter, the secondary throat radius (r_p). In this way, the bimodal porous medium has main throats with a greater radius (r_i) and secondary throats with a lesser radius (r_p). Fig. 1c shows the modified bimodal porous medium proposed in this study to represent the intracellular space of plant-based food material. In Fig. 1c, four rectangular portions are removed from the center of the secondary pore bodies to represent the intracellular space of plant-based food material. Therefore, a fourth characteristic parameter was added to define cell wall thickness (L_w) and thus establish the intracellular space dimensions (rectangular portion).

3. Materials and methods

3.1. PDMS micromodel fabrication procedure

The PDMS micromodels were built in three steps. The first step involved developing the pattern design (photomask) with a given pore size distribution. The second step obtained the photopolymer mold (master). The final step molded the PDMS layers and their adhesion to obtain a finished PDMS micromodel. The manufacturing method of the PDMS micromodels and some modifications of the procedure used to design and fabricate microfluidic systems developed by Duffy et al. (1998) are described in detail below.

3.1.1. Pattern design

On the base of the modified bimodal porous medium approach, two types of micromodels were built to represent two types of cell microstructure. The type 1 micromodels represent the microstructure of fresh plant-based food material, and type 2 micromodels represent a damaged microstructure. A pattern design for each type of micromodel was developed. The values of r_i (main throat radius representing intercellular space), r_p (secondary throat radius representing plasmodesmata), and L_w (solid portion of a given thickness representing the cell wall) were obtained from three pore size distribution functions $f(r)$ through a code in Microsoft Visual Basic (version 6.3.8863). These pore size distributions functions were normal type, as are those reported for apple microstructure (Herremans et al., 2015; Rahman et al., 2018a,b). Each normal pore size distribution function had five parameters, which are minimum radius (r_{min}), maximum radius (r_{max}), mean radius ($\bar{r}$), standard deviation (σ), and number of radius values (N). Thus, each normal pore size distribution function was defined as $f(r) = f(r_{min}, r_{max}, \bar{r}, \sigma, N)$. To design and build the PDMS micromodels, the proportion and dimension of the cell structures had to be expanded from their experimental measured values to obtain good resolution patterns, and allows it construction, and visualization of the liquid inside the micromodels during drying. The parameters used to feed the Microsoft Visual Basic code are shown in Table 1. The number of radius values (N) was estimated by Eqs. (1)–(3).

The number of main throat radius values (Nr_i) was calculated by Eq. (1) where N_x and N_y are the number of nodes or pore bodies on the x and y axes, respectively (see Fig. 2a). Patterns (photomasks) of 20 × 20 nodes were built in the present study. Thus, 840 values of the main throat radius generated the intercellular space.

$$Nr_i = 2N_xN_y + N_x + N_y \tag{1}$$

The number of secondary throat radius values (Nr_p) was determined by Eq. (2). In the 20 × 20 node pattern, the plasmodesmata originated from 1764 values of the secondary throat radius.

$$Nr_p = 4 * (N_x + 1) * (N_y + 1) \tag{2}$$

The number of wall thickness values (NL_w) was calculated by Eq. (3). In the 20 × 20 node pattern, 840 wall thickness values produced the cell wall.

$$NL_w = 2N_xN_y + N_x + N_y \tag{3}$$

The Visual Basic code generated a three-column table for both types of patterns with the parameters that were entered. Each table contained a data set size to represent intracellular space, plasmodesma, and the cell wall and was then used by a Microsoft Visual Basic subroutine that automatically allowed drawing the necessary patterns with the AutoCAD software (version R.17.0.540, Autodesk Inc.). For both types of patterns, the pore-body-center to pore-body-center distance (L) was 3 mm. Each type of drawn pattern was then printed on a transparent acetate sheet (3 M transparency film, CG3460) with an Ink Jet Printer (Canon, Pixma iP4910). All printed patterns were independently stored until later use. An example of a 20 × 20 node pattern is shown in Fig. 2b, which is similar to patterns designed and printed in the present study.

3.1.2. Developing the photopolymer mold (master)

Fig. 3 describes the PDMS micromodel fabrication procedure from the pattern design described in the previous section. The flowchart illustrated in Fig. 3 shows the development of the photopolymer mold (master) and considers PDMS layer preparation and subsequent adhesion.

Table 1
Statistical parameters used for the pattern design of each type of micromodel where r_{min}, r_{max}, and $\bar{r}$ are the minimum, maximum, and mean radius, respectively, σ is the standard deviation, and N is the number of generated radius values.

Cellular tissue structure	Symbol	Pattern type	r_{min}, μm	r_{max}, μm	$\bar{r}$, μm	σ, μm	N
Intercellular space	$f(r_i)$	1	110	310	210	50	840
		2	110	310	210	50	840
Plasmodesma	$f(r_p)$	1	70	100	85	10	1764
		2	90	120	105	10	1764
Cell wall	$f(L_w)$	1	400	600	500	50	840
		2	400	600	500	50	840

The procedure to obtain the photopolymer mold includes several steps. First, a 10-cm photopolymer square plate (TOYOBO model KM43GS) and a printed pattern (10-cm acetate square sheet), such as the one shown in Fig. 2b, were used to build the mold for the PDMS porous layer. Two pieces of clean flat glass (12 × 12 × 0.4 cm) and four binder clips were necessary to produce the assembly shown in Fig. 3a. The assembly was placed in the UV light chamber (containing three F6T5/BLB tubes) for 17 min at a wavelength of 365 nm. The assembly was later disassembled and the photopolymer plate washed with water at room temperature for 7 min (see Fig. 3c). The wash water was drained from the photopolymer plate surface and the photopolymer plate mold was re-exposed to UV light for17 min to strengthen the developed pore network (master). The depth of all pores and throats in the finished photopolymer molds were approximately 210 μm according to the photopolymer depth layer of the TOYOBO KM43GS plate.

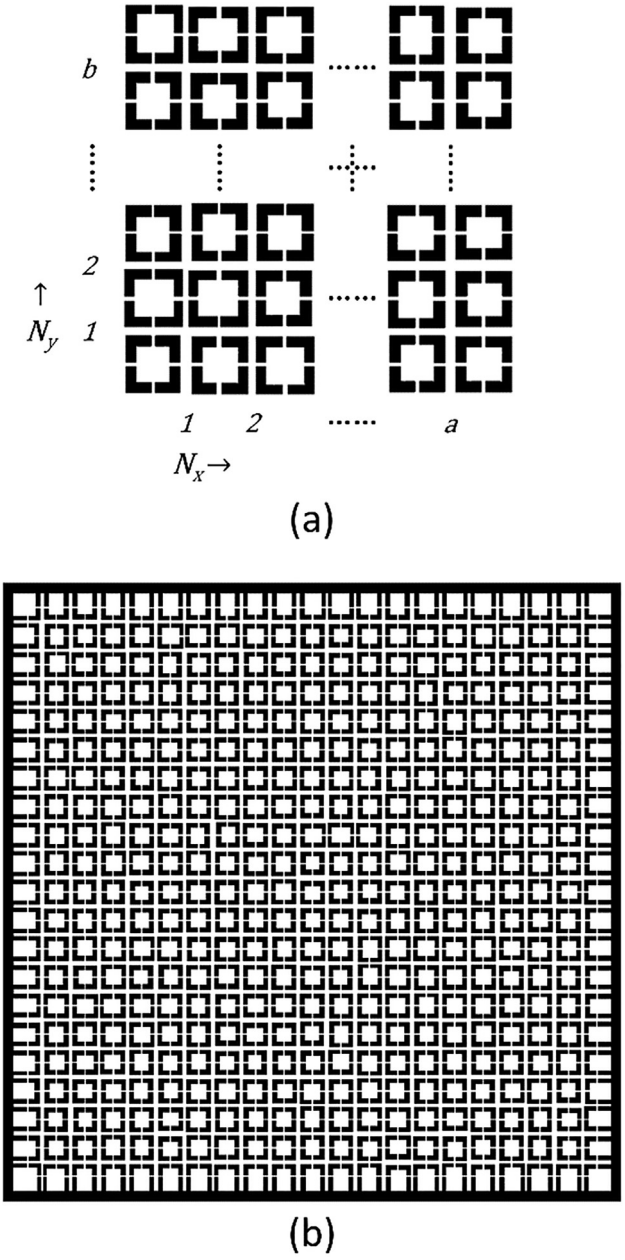


Fig. 2. Examples of patterns applying the plant tissue approach. (a) $a \times b$ node pattern and (b) 20 × 20 node pattern used to build the micromodels. The intercellular space, plasmodesmata, and intracellular space are represented in white, while the cell walls and pattern contours are represented in black.

3.1.3. Molding and adhesion of PDMS layers

The following was the procedure to prepare the PDMS layers and their subsequent adhesion. Prior to the procedure, 36 ml of Sylgard® 184 silicone elastomer (Dow Corning Corporation, Midland, U.S.A) was mixed at a 10:1 ratio (elastomer base:curing agent) for 5 min in a Petri dish. To remove the bubbles produced by shaking the mixture, vacuum pulses were applied (6.4 kPa at 20 °C). To obtain a PDMS porous layer, half the PDMS was poured into a glass cuvette (12 × 12 cm). The glass cuvette was made of a photopolymer mold, a clean glass (12 × 12 × 0.4 cm), four rectangular clean glass pieces (10.5 × 1.5 × 0.4 cm), and eight binder clips as shown in Fig. 3e. To obtain a PDMS flat layer (without pores), a procedure similar to the one described above was carried out; however, in this case, a new glass cuvette (12 × 12 cm) without the photopolymer mold was used (see Fig. 3f).

Both porous and flat PDMS layers were later cured at 85 °C for 35 min in an oven at a controlled temperature (Jeio Tech, model OV-12). After the PDMS curing process, PDMS layers (porous and flat) were unmolded (PDMS peeled from glass cuvettes) and treated by cold plasma (Plasma Cleaner PDC-002, Harrick Plasma) to allow the irreversible adhesion between both PDMS layers. The cold plasma treatment conditions were low pressure (27 – 40 Pa), controlled airflow (12 ml min^{-1}), high power (26.9 W), and 30-min treatment time. Both PDMS layers were joined and placed between two clean flat glass pieces (12 × 12 × 0.4 cm), and the assembly (PDMS layers and flat glass) was placed in an oven at 90 °C and pressed with a mass of 1.5 kg for 3 h as shown in Fig. 3i. All the flat glass used in the micromodel fabrication procedure was conditioned according to the methodology described by Díaz et al. (2011). An irreversible bonding of both PDMS layers was achieved by applying these procedures. Approximately 5-mm surplus edges were removed from each side of the completed PDMS micromodel. All finished PDMS micromodels had an approximate thickness of 4 mm. Finally, the completed PDMS micromodels were labeled and stored independently in polyethylene bags until later use.

3.2. Isothermal drying experiments

The finished PDMS micromodels were used in isothermal drying experiments at 20 °C, atmospheric pressure, and approximately

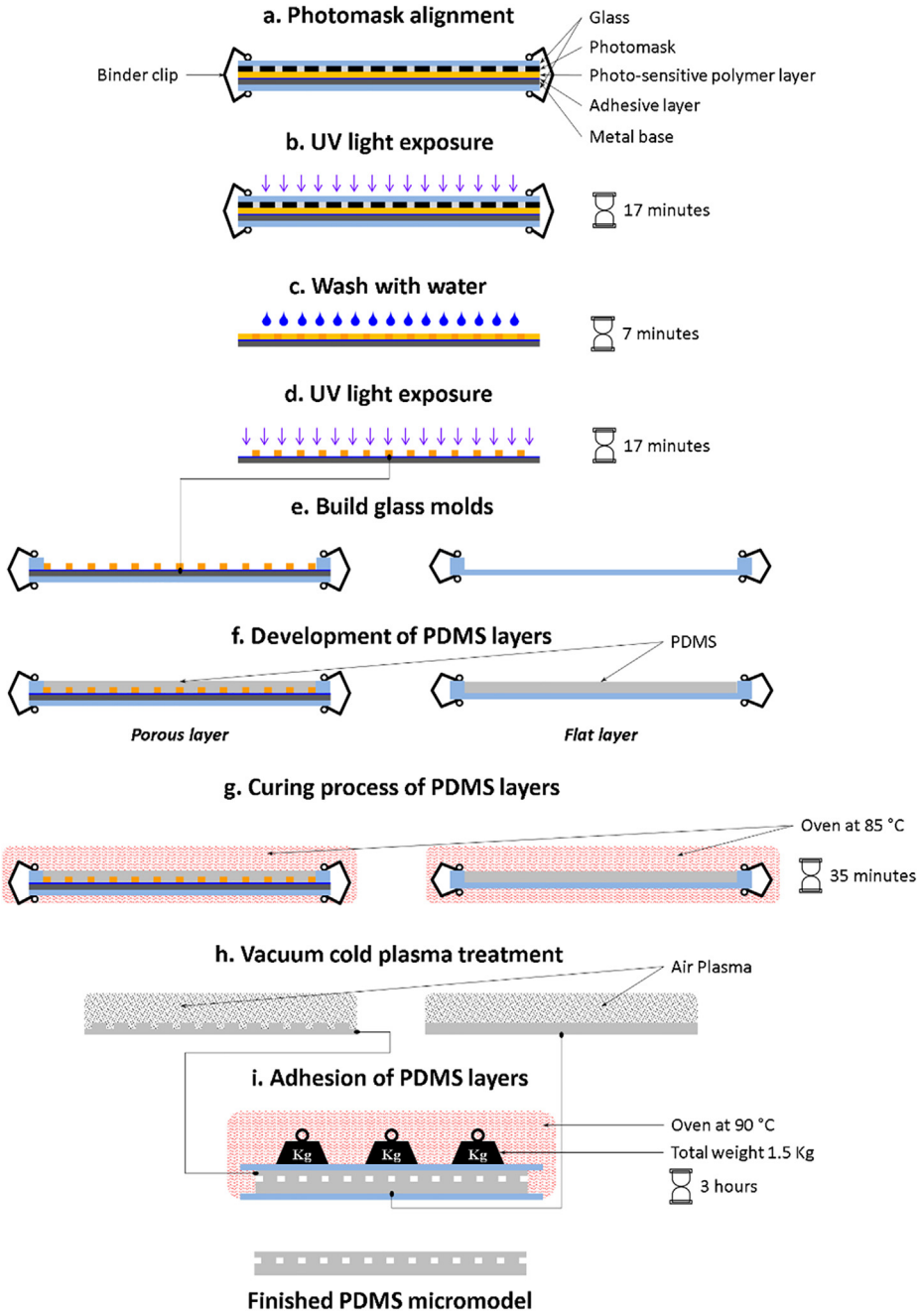


Fig. 3. Flowchart of the polydimethylsiloxane (PDMS) micromodel building process from the pattern design (photomask). (For the interpretation of the references in this figure legend, the reader is referred to the web version of this article.)

40% relative air humidity. The setup of all isothermal drying experiments is shown in Fig. 4. A fluorescent dye (pyranine: 8-Hydroxy pyrene-1,3,6-trisulfonic acid trisodium salt, Sigma-Aldrich) aqueous solution was used to visualize and record the drying front. Firstly, the top of each finished PDMS micromodel was cut just before vacuum impregnation to avoid water condensation or pollution in the porous medium. PDMS micromodels were vacuum impregnated with pyranine aqueous solution (2.64 g L^{-1}) at 20 °C and 6.4 kPa according to the methodology proposed by Badillo et al. (2011). After vacuum impregnation, the excess of pyranine aqueous solution was removed from the micromodel surface with absorbent paper. The impregnated micromodel was immediately placed on a precision balance (Radwag, model PS 510/C/1) to start the isothermal drying experiment. The measurement range of the balance was 0–510 g with an accuracy of 0.001 g. The PDMS micromodels were arranged horizontally during the drying process to avoid the influence of the gravitational force. The open side of each PDMS micromodel corresponds to their top, meanwhile the bottom and left and right sides were closed during PDMS layer adhesion, and were therefore considered impervious.

During the drying process, the weight changes of each PDMS micromodel were recorded at 1-min intervals with a desktop computer. The PDMS micromodel was permanently illuminated with a UV light system (F6T5/BLB tube), and the pyranine aqueous solution configuration inside the porous medium (drying front morphologies) was recorded with a digital camera (Genius, model WideCam F100). Digital camera was equipped with a 1080p Full HD pixel CMOS image sensor, the lens was adjusted manually,

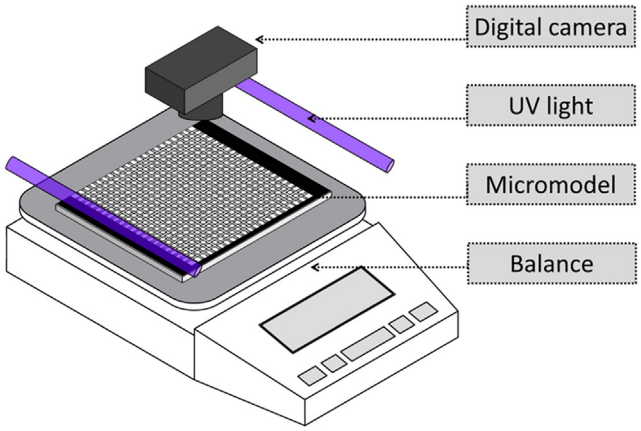


Fig. 4. Setup of isothermal drying experiments using PDMS micromodels.

and the resolution used in the record of the drying fronts was 1920 × 1080 pixels. The images captured by the digital camera were collected with the Video velocity software (version. 3.6.2008.0, CandyLabs Home). In the Video Velocity software, device properties were configured as follows. (*i*) Video processor amplifier: brightness −40, contrast 30, hue −2000, saturation 50, sharpness 5, gamma 140, white balance 5500, and backlight compensation 0. (*ii*) Camera control: exposure −5, and low light compensation off. The device properties adjust allowed proper monitoring of drying fronts. Images and weight changes data recorded from each PDMS micromodel drying experiment were used to analyze the drying fronts and elaborate typical drying curves using the classical methodology described by Barbosa-Cánovas and Vega-Mercado (1996) with some modifications.

3.3. Statistical analysis

An analysis of variance (ANOVA) was applied at a significance level of $\alpha \leq 0.05$ was carried out by means of STATGRAPHICS Centurion software version 16.1.03 (Statpoint Technologies, Inc., Warrenton, Virginia, USA). The independent variables analyzed (factors) were micromodel type which correspond to 1 and 2, and drying time that correspond to 0, 30, 60, and 90 h. The effects of micromodel type, drying time, and their interactions on the value of pyranine aqueous solution saturation were considered. Pyranine aqueous solution saturation (S_l; %) was calculated according to Eq. (4).

$$S_l = (M_t - M_{DM}/M_0 - M_{DM}) * 100 \quad (4)$$

where M_t, M_{DM}, and M_0 are partially liquid filled micromodel weight (g) at time = t, dry micromodel weight (g), and completely liquid filled micromodel weight (g), respectively.

The Tukey's HSD test was applied (where appropriate) to estimate differences between pyranine aqueous solution saturation values at a confidence level of 95%. Quantitative results were plotted using SigmaPlot software version 12.0.0.182 (Systat Software, Inc., San Jose, California, USA).

4. Results and discussion

A new pattern of porous medium has been developed in the present study that can simulates the structure of plant-based food material commonly subjected to drying. The proposed porous medium approach can contain a greater amount of liquid compared with monomodal and bimodal porous media (see Fig. 1) because a rectangular void section surrounded by four walls replaced the solid portions of the monomodal porous medium. In this new approach, small throats have been incorporated through the cell walls to ensure the hydraulic connectivity of porous media. The application of this new artificial porous medium mimicked four important components of plant-based food material, such as intracellular space, plasmodesma, cell wall, and intercellular space. In future studies, a greater number of plasmodesmata (throats crossing the cell walls) for each cell of the pattern could be considered to incorporate a greater number of elements in the design and construction of micromodels; this would achieve better representation of the plant-based food material.

4.1. Polydimethylsiloxane (PDMS) micromodel fabrication procedure

The procedure to build PDMS micromodels was described in Section 3 and Fig. 3 summarizes it graphically. We considered two types of micromodels to represent two cellular types of microstructures. Fig. 5 illustrates the pore size distribution of three plant tissue structures incorporated in the pattern design for both types of micromodels. It is possible to observe in Fig. 5 that pore size distribution functions that define intercellular space and the cell wall were equivalent for both types of micromodels. Therefore, the difference between the two types of micromodels lies in the mean radius value of the normal pore size distribution function defined by the plasmodesma ($\bar{r_p}$). Table 1 reveals that the pore size distribution functions in type 1 micromodels that define the plasmodesma (r_p) and intercellular space (r_i) do not overlap, that is, $f(r_p) < f(r_i)$.

The type 1 micromodel represents the microstructure of fresh plant-based food material in which there is a great difference between r_p and r_i values. On the other hand, the pore size distribution functions $f(r_p)$ and $f(r_i)$ in the type 2 micromodel overlapped for some r_p and r_i values and $f(r_p) \leq f(r_i)$. The type 2 micromodel represents a modified microstructure that originated when a given plasmodesma had a larger diameter than some main throats representing intercellular space.

It is known that fruit and vegetable microstructures change during storage or when they are treated prior to the drying process (Aguilera, 2005; Cen et al., 2013; González-Fésler et al., 2008; Lewicki, 2006; Ramirez et al., 2011). Microstructure changes can be established by intercellular space and cell diameter size modification or cell wall disruption (Cen et al., 2013; Herremans et al., 2015; Ramirez et al., 2011; Varela et al., 2007; Vicent et al., 2017). Khan et al. (2017, 2018a, 2018b) and Rahman et al. (2018b) reported that the cell membrane collapse of potatoes and apples occurs at different stages of drying, and corresponds to a progressive process controlled by temperature. In our study, the throats crossing the cell walls represent the plasmodesmata, but the presence of these small throats could also be justified by channels formation due to cell wall disruption or collapse induced by extensive storage, treatment prior to the drying, or the effects of temperature and moisture gradients during drying process.

The building procedure of PDMS micromodels is shown in Fig. 3; it is more efficient for micromodel molding than the techniques used to build glass and resin micromodels (Badillo et al., 2011; Bonnet and Lenormand, 1977; Cortés et al., 2014; Díaz et al., 2011). Using the new porous medium approach, and modified photolithography technique applied in the present study, it was possible to obtain PDMS micromodels that capture the essence of plant-based food material.

Fig. 6 shows a type 1 PDMS micromodel and highlights its transparency, deformability, and good resolution. Fig. 6c was obtained with an Optech optical microscope (model LFZ s7n 200092, Munich, Germany), equipped with an Opticam camera. The research group led by Professor Segura-Ponce had previously used the photolithographic technique developed by Duffy et al. (1998)

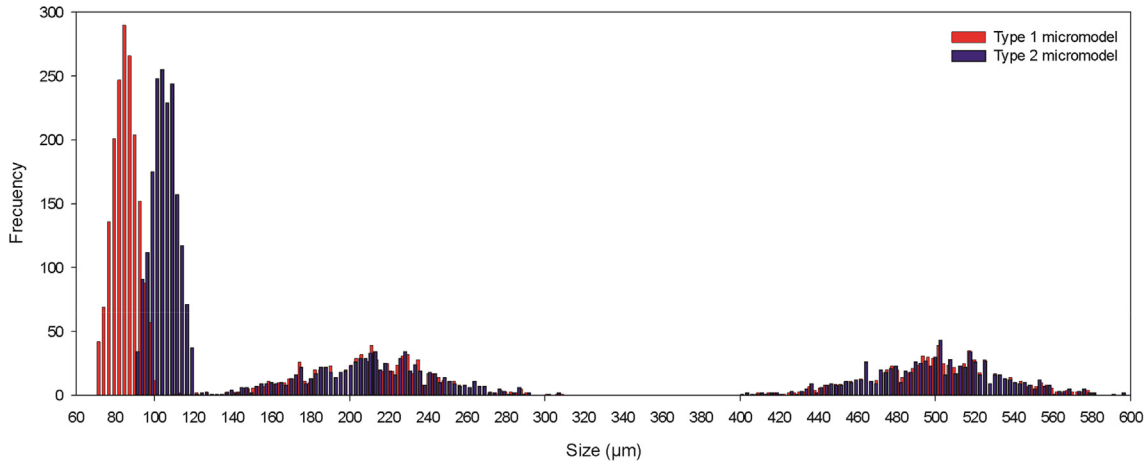


Fig. 5. Pore size distributions for both completed types of micromodels. Each pore size distribution describes radius values of the plasmodesma (r_p), intercellular space (r_i), and cell wall (L_w) from left to right, respectively. (For the interpretation of the references to color in this figure legend, the reader is referred to the web version of this article.)

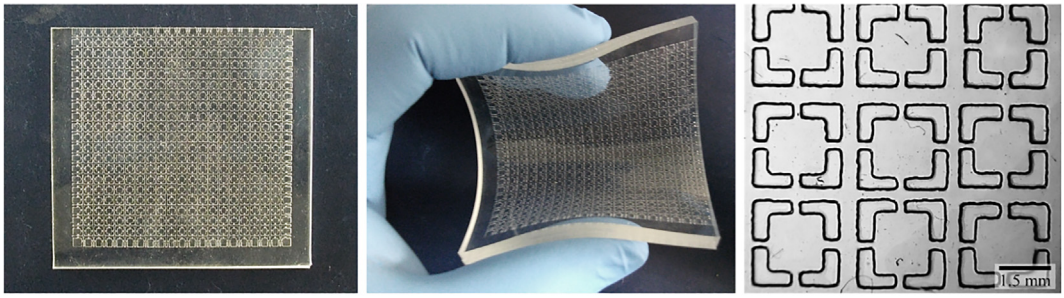


Fig. 6. Type 1 polydimethylsiloxane (PDMS) micromodel built in the present study. (a) General view of micromodel, (b) micromodel deformability, and (c) zoom in of micromodel with an optical microscope.

and incorporated some modifications to obtain 2D and 3D PDMS micromodels (Segura et al., 2013, 2015). A relevant aspect of this methodology is that when using the Toyobo-KM43GS photopolymer plate, a homogeneous depth of pores and throats was achieved when developing the PDMS micromodels. The photopolymer plate used in the present study provided a constant depth of 210 μm.

4.2. Isothermal drying experiments

The finished PDMS micromodels were used in isothermal drying experiments developed in accordance with the methodology described in Section 3.2. Analysis of drying dynamics and possible drying mechanisms were developed. Fig. 7 displays two average drying curves obtained from six drying experiments, three for both types of PDMS micromodels. Each curve was fitted by a fifth order polynomial curve with the OriginPro software (version 8.5.0, OriginLab Corporation) to make it easier to determine the drying rate. Fig. 7 shows a constant decrease in moisture content for both types of PDMS micromodels as the isothermal drying process progresses. The analysis of variance reported that both considered factors had significant effects on pyranine aqueous solution saturation values ($p < 0.05$), i.e., statistical differences in the pyranine aqueous solution saturation values were observed for each micromodel type (micromodels type 1 and 2) and drying time analyzed (0, 30,60, and 90 h of drying process). The Tukey's HSD test stated that after 60 h of drying time there were significant differences in pyranine aqueous solution saturation values for both micromodel types. Meanwhile, no significant differences in pyranine aqueous solution saturation values were found between both micromodel types at the beginning of drying (0 h), and after 30 and 90 h of such process. Obviously, each drying time considered in this study produced significant differences in pyranine aqueous solution saturation values, i.e., 0 h ≠ 30 h ≠ 60 h ≠ 90 h. Fig. 7 shows that the drying curves of both types of PDMS micromodels have the typical behavior of a porous medium such as plant-based food material. Fig. 7 demonstrates that the drying time of type 2 micromodels was shorter than for type 1 micromodels, with a mean value of 96.5 ± 0.71 h and 110 ± 1.41 h, respectively.

Ramirez et al. (2011) found that the main factor affecting the drying rate is the cell wall rupture induced by the pre-treatment of the apple plant tissue, such as immersion in boiling water, vacuum impregnation, and freezing/thawing. The drying curve behavior of our experiments agreed with the trend observed by Ramírez et al. (2011) in which the drying rate was higher for the treatments that produced greater damage to the apple cell wall. Given that type 2 micromodels consisted of larger diameter throats crossing the cell wall (plasmodesmata), type 2 micromodels dried more quickly than type 1 micromodels. This statement agrees with the results reported by Khan et al. (2018b) and Rahman et al. (2018b) for the drying apples (*Granny Smith*) at lower drying air temperature (45 and 50 °C). These authors point out that cell membrane rupture in apple samples did not occur due to the lower drying air temperature, i.e. apple microstructure was kept like fresh cellular tissue. Therefore, a slower drying process was observed compared to the experiments carried out at higher temperatures (60 and 70 °C) where significant cell membranes rupture occurs.

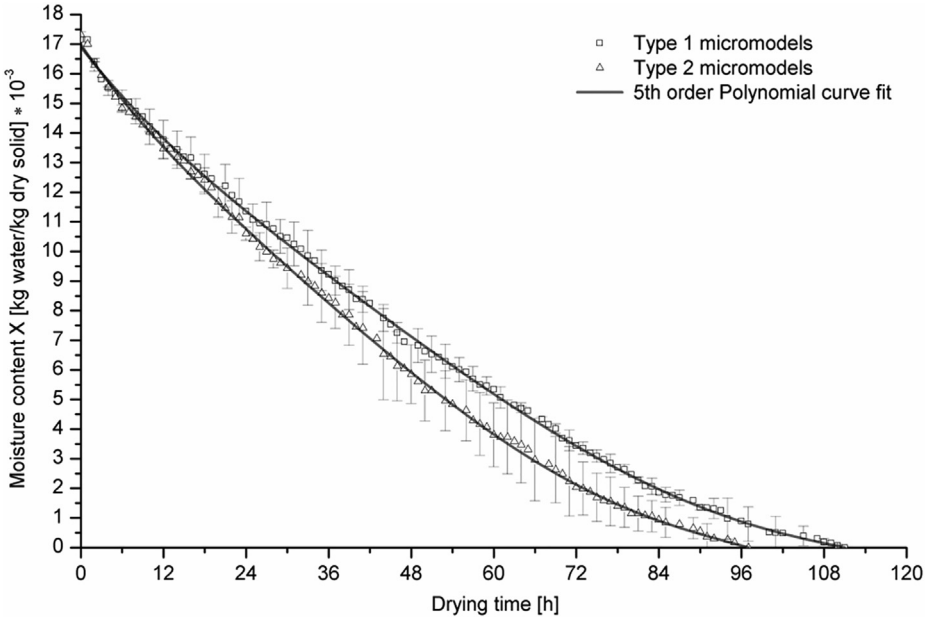


Fig. 7. Average drying curves for both types of polydimethylsiloxane (PDMS) micromodels.

Fig. 8 displays various drying front morphologies for both types of PDMS micromodels built in the present study. The drying fronts were recorded at different values of pyranine aqueous solution saturation to visualize their behavior at different drying stages.

The drying front behavior was similar for both types of PDMS micromodels. The cells represented in the type 2 micromodels were more accessible to drying compared with cells of type 1 micromodels. This is justified by the overlap of the pore size distribution functions that define the plasmodesma (r_p) and the intercellular space (r_i) in type 2 micromodels, that is, $f(r_p) \leq f(r_i)$. Capillary forces govern isothermal drying in a porous structure; therefore, drying is a hierarchical process where the larger throats dry before smaller ones (Laurindo and Prat, 1996; Segura, 2007; SanMartin et al., 2011). Drying front images, such as those in Fig. 8, show that when the radius value of a given plasmodesma is greater than the radius value of the main throat being dried, drying continues through the intracellular space before continuing to dry the main throat with a smaller radius.

It was expected that the drying front would be more regular for type 2 micromodels; however, no great differences were observed in drying front morphologies for both types of micromodels. This can be justified by the random nature of the porous media. Micromodel patterns were drawn from random pore size distributions, and there was a low probability that a plasmodesma would have a radius value greater than that of a main throat (intercellular space). In the type 2 micromodels, there were 569 plasmodesmata in the interval between 109.57 and 122.76 μm (secondary throat radii), while only six main throats defining the intercellular space were in the same interval. A greater overlap between $f(r_i)$ and $f(r_p)$ can be obtained by using higher standard deviations (σ) values or similar mean radius values, that is, $\bar{r}_i \cong \bar{r}_p$.

SanMartin et al. (2011) reported drying simulations of a monomodal and non-hygroscopic porous medium saturated with pure water and diluted sucrose solutions. The authors clearly observed three regions inside the porous medium during drying: dry region, partially saturated region, and completely saturated region. The drying fronts shown in Fig. 8 are similar to those presented by SanMartin et al. (2011). Nevertheless, during most of the drying time, only the partially and completely saturated regions were observed in both types of PDMS micromodels. SanMartín et al. (2011) showed that the presence of compact drying fronts is strongly influenced by the fast drying rate period at the early drying stage. In our study, as described below, the fast drying rate period did not occur, so that a rough front was observed from the beginning of drying (see Fig. 8).

Fig. 9 displays the drying rate (R) curves and derivative of drying rate (R') curves for both types of PDMS micromodels. The drying rate was obtained from the derivative of the moisture content (X, kg water/kg dry solid) with respect to the drying time (t, s). The derivative of the drying rate (R') was obtained from the second derivative of X with respect to t, that is, $R = \frac{dX}{dt}; R' = \frac{d^2X}{dt^2}$. Both determinations were performed using data generated from the fifth order interpolation polynomial for 1-hr time intervals.

Fig. 9 shows that the drying rate of type 2 micromodels was higher than for type 1 micromodels. For both types of micromodels, only the slow drying rate period was observed because the drying experiments occurred at a low drying air temperature (20 °C), which in turn led to a low evaporation rate. At higher drying air temperatures (>20 °C), the water evaporation rate is faster; a great deal of liquid water is drained toward the porous medium surface where it is evaporated and causes a marked change in the drying curves. Thus, drying time decreased and the behavior of the drying rate curves also changed.

Metzger et al. (2007) performed drying simulations of various unimodal and bimodal porous media at low temperatures and under isothermal conditions. These authors reported that the fast drying rate period is only given by air drying conditions and outer geometry of the porous body; this rate is identical to the evaporation rate of a liquid surface in spite of the structural properties of the material. They also pointed out that the porous structure determines how long the initial drying rate can be maintained and how it will decrease during the so-called second drying period (falling rate drying period). The falling rate period is a result of liquid cluster evaporation, so the continuous phase is poorly connected to the evaporation surface (Segura and Toledo, 2005).

The behavior of R and R' indicated in Fig. 9 clearly allows establishing three drying stages for both types of micromodels. At the beginning of the first drying stage (A), the liquid saturating the throats, pores, and cells near the open side of the micromodels was quickly removed, producing a peak in R' of approximately

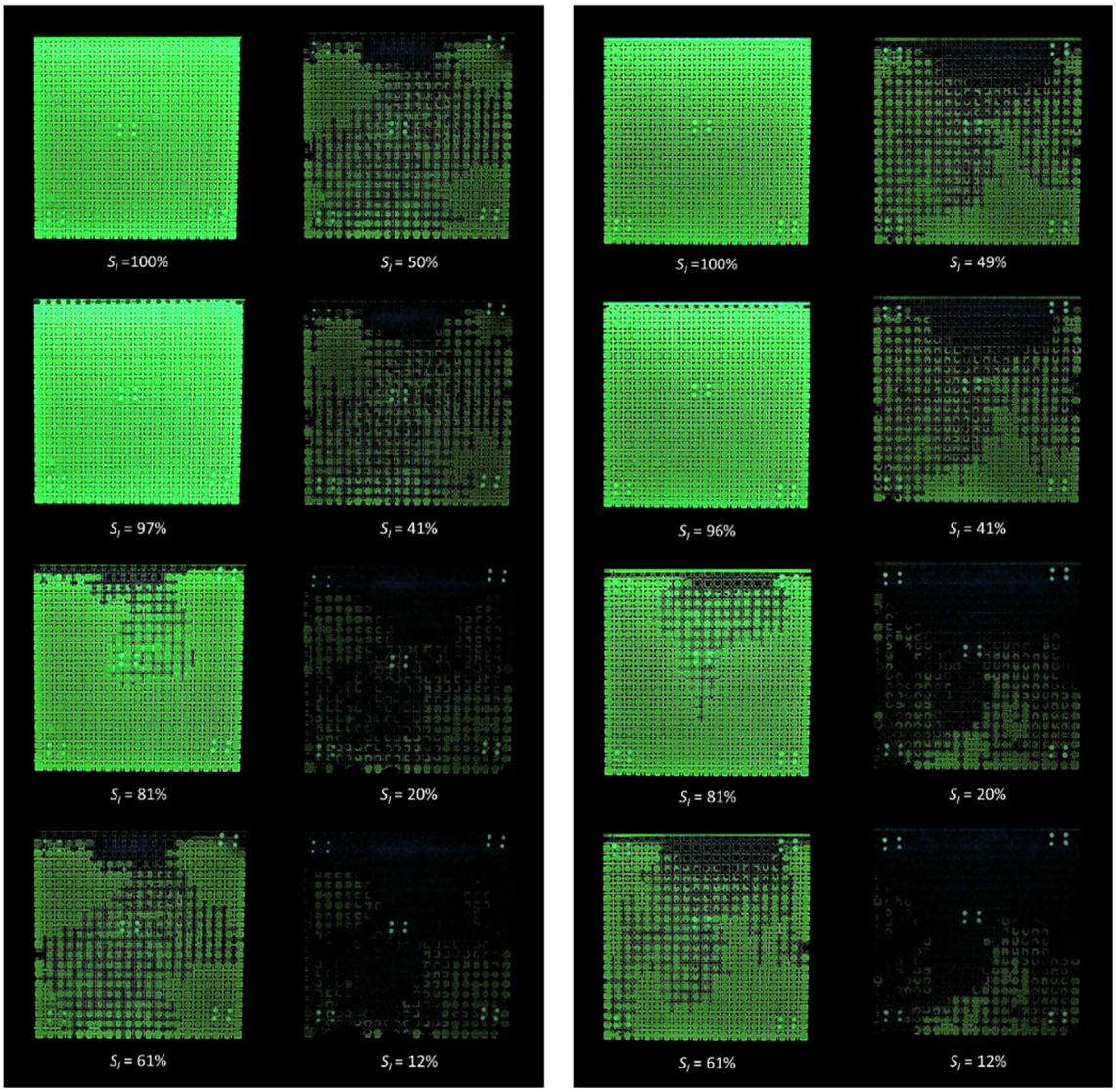


Fig. 8. Drying front morphologies for both types of polydimethylsiloxane (PDMS) micromodels at different pyranine aqueous solution saturation (S_l) values. Black regions represent air-water vapor mixtures, and green regions correspond to the pyranine aqueous solution. The image sequence on the left corresponds to the type 1 micromodel, and the image sequence on the right corresponds to the type 2 micromodel. (For the interpretation of the references to color in this figure legend, the reader is referred to the web version of this article.) (For interpretation of the references to color in this figure legend, the reader is referred to the web version of this article.)

97% liquid saturation (see Figs. 8 and 9). The first drying stage was approximately between 17×10^{-3} and 12×10^{-3} (kg water/kg dry solid), equivalent to 100% to 71% liquid saturation, respectively. In the first drying stage, 29% moisture content was eliminated by drainage and surface evaporation sequences and internal evaporation. At this point, R reached maximum values for both types of micromodels. Drainage lasts as long as there is hydraulic connectivity within the porous medium. The liquid-filled pores and throats and liquid films in the corners of the pores provide the hydraulic connectivity of the porous network (Segura and Toledo, 2005). Since the experiments were carried out at room temperature (20 °C), at atmospheric pressure, and there were no thermal gradients through PDMS micromodels, only moisture gradient controlled the isothermal drying process. The vapor partial pressure difference between gas and liquid phases allows the removal of liquid water from PDMS micromodel. Prat, Laurindo, Segura and coworked provide a detailed review about compute of vapor partial pressure in diverse porous medium. The authors included in their papers a detailed methodology to solve the pressure field on the porous network during drying (Laurindo and Prat, 1996; 1998; Prat, 1993; Segura and Toledo, 2005; Segura, 2007).

In the second stage (B), a pseudo-period of constant drying rate was observed for both types of micromodels approximately between 12×10^{-3} and 5×10^{-3} (kg water/kg dry solid), respectively. During the pseudo-period of constant drying rate, the drying front morphologies were similar to those shown in Fig. 8 for S_l values between 71% and 30%. The pseudo-period of constant drying rate was originated by the simultaneous elimination of moisture content through drainage (from the intercellular space) and internal evaporation from the cells near the open side that were more accessible to drying (plasmodesmata with a greater radius).

As drying progresses, the moisture content of the intercellular spaces was gradually eliminated; this caused the loss of hydraulic connectivity of the porous medium; therefore, internal evaporation controlled the drying of PDMS micromodels. Fig. 8 shows that the loss of hydraulic connectivity occurs at liquid saturations < 61% for both types of micromodels. Porous medium disconnection caused the formation of islands (liquid clusters), which dried indepen-

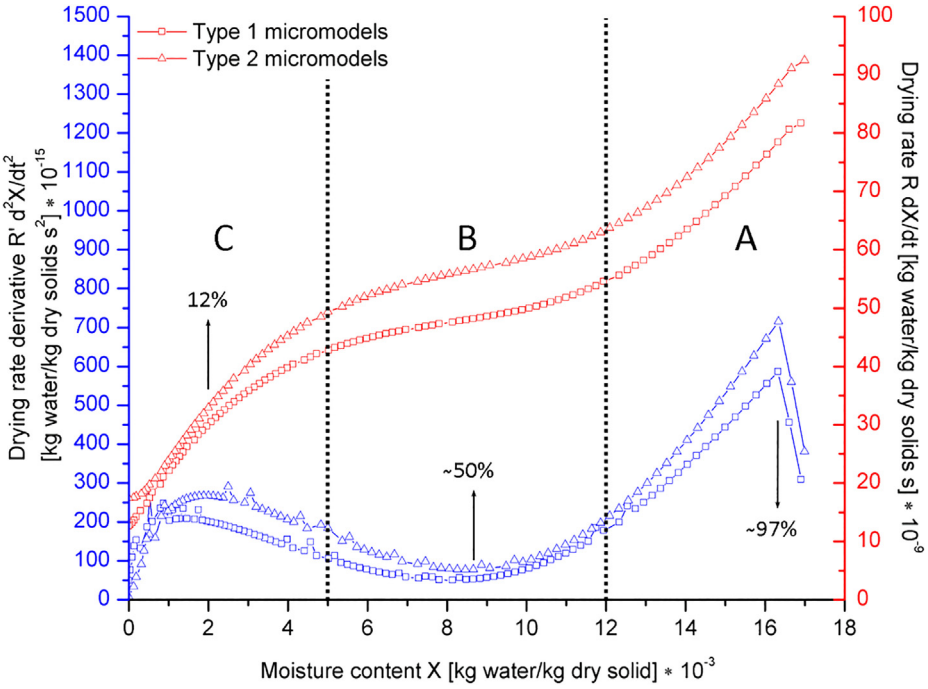


Fig. 9. Drying rate curves and drying rate derivative for both types of polydimethylsiloxane (PDMS) micromodels. (For the interpretation of the references to color in this figure legend, the reader is referred to the web version of this article.)

dently one from the other by internal evaporation. The liquid clusters near the open side of the micromodel evaporated first, allowing the advance of the drying front through the porous medium. Fig. 9 highlights a minimum value for *R'* of approximately 50% liquid saturation. At this point, the loss of hydraulic connectivity and the increase in island formation (see Fig. 8) led to a decrease in the drying rate, which preceded the last drying stage. In the last drying stage (C), moisture content was slowly removed by internal evaporation because the liquid remained inside the individual cells or in isolated groups of cells (liquid clusters). It originated an attenuated peak in *R'* in the last drying stage for both types of micromodels. In the last drying stage, water vapor was slowly removed from the micromodels because the drying front was the furthest from the open side for both types of micromodels. The drying front morphologies of the last drying stage were similar to those shown in Fig. 8 for liquid saturation values $\leq$ 20%.

When the drying process finished, a small amount of pyranine in the solid state was deposited in the regions closest to the open side of both types of micromodels (unpublished data). The absence of a considerable amount of pyranine in the regions further away from the open side of the micromodels indicates that drainage and surface evaporation sequences had a greater participation during the early drying stages. In the last drying stage, pyranine was deposited in the same regions where it was when the water evaporated, that is, this fluorescent dye was not drained to the surface as observed in the first drying stages for both types of micromodels.

According to results by Metzger et al. (2007) when the microstructure ratio between macro- and micro-channels constituting the type 2 bimodal porous medium is $\approx$ 2.5 (40:100 μm, with σ 2 and 5 μm, respectively), the micro-channels (liquid clusters) do not provide liquid water to macro-channels that had been previously dried. The results of our study agree with simulations by Metzger et al. (2007) for the drying of type 2 bimodal porous medium. On the other hand, according to the microstructure characterization of the apple plant tissue, the ratio between the intracellular space, 220 μm (Rahman et al., 2018a,b), and the plasmodesma, 0.05 μm (Defraeye et al., 2016; Jeffery et al., 2012), is approximately 4,400. This microstructure ratio is enormous compared with the ratios used in our study (2.47) and the work by Metzger et al. (2007). Therefore, we postulate that the drying of porous media, such as plant-based food material, at low air temperatures and under isothermal conditions is a completely hierarchical process in which internal evaporation could be the predominant drying mechanism.

Convective drying studies of plant-based food material are frequently developed at air temperatures that are higher than those used in our experiments (>20° C). However, Bai et al. (2002) reported that drying can be carried out even at 0 °C as long as the relative air humidity is low. Extensive drying periods, high shrinkage, and quality deterioration of dried products are some disadvantages of drying at low air temperatures. In the present study, the micromodel construction and drying experiments have demonstrated that porous medium architecture defines the liquid and vapor phase behavior during drying. When a porous medium is comprised of two pore size distributions that generate macro- and micro-channels, the macro-channels are first dried by forming liquid clusters (micro-channels saturated with liquid), and the micro-channels are then dried. Although the PDMS micromodel implies a simplification of both the microstructure and set of phenomena that occur in plant-based food material during a real drying process, it is a good tool for understanding the drying dynamics of porous media with an architecture that is similar to that of plant-based food material.

5. Conclusions

In this research study, we proposed a new pattern of porous medium that can simulates the structure of plant-based food material commonly subjected to drying. In turn, we built polydimethylsiloxane (PDMS) micromodels using the modified photolithographic technique with a TOYOBO-KM43GS photopolymer plate. The use of a pyranine aqueous solution (2.64 g L^{-1})

and constant UV illumination allowed the drying profiles of the PDMS micromodels to be observed as the drying process advanced. The drying rate of type 2 micromodels was higher than for type 1 micromodels. This behavior demonstrated that drying kinetics is strongly dependent on porous medium architecture and pore size distribution. The drainage and surface evaporation sequences and internal evaporation governed PDMS micromodel drying, but internal evaporation was the predominant drying mechanism throughout the process. Our results show that micromodels are a powerful tool to study drying mechanisms from which researchers can recreate various cell structures of plant-based food material and observe their effects on drying kinetics. The PDMS micromodels could be applied to study several processes that involve mass transfer in plant-based food material. Future research should be developed to study the behavior of PDMS micromodels during non-isothermal drying processes, and use solutions closer to the plant-based food composition.

Declaration of Competing Interest

The authors declare that they have no known competing financial interests or personal relationships that could have appeared to influence the work reported in this paper.

Acknowledgments

This work was supported by the Universidad del Bío-Bío [Scholarship fund for postgraduate research], the INNOVA BIOBIO [16IP-65192 project], and the Fondef Idea [project N° ID16I10206].

Appendix A. Supplementary material

Supplementary data to this article can be found online at https://doi.org/10.1016/j.ces.2019.115385.

References

Aguilera, J.M., 2005. Why food microstructure?. J. Food Eng. 67 (1–2), 3–11. https://doi.org/10.1016/j.jfoodeng.2004.05.050.

Badillo, G.M., Segura, L.A., Laurindo, J.B., 2011. Theoretical and experimental aspects of vacuum impregnation of porous media using transparent etched networks. Int. J. Multiphase Flow. 37 (9), 1219–1226. https://doi.org/10.1016/j.ijmultiphaseflow.2011.06.002.

Bai, Y., Rahman, M.S., Perera, C.O., Smith, B., Melton, L.D., 2002. Structural changes in apple rings during convection air-drying with controlled temperature and humidity. J. Agric. Food Chem. 50 (11), 3179–3185. https://doi.org/10.1021/jf011354s.

Barbosa-Cánovas, G.V., Vega-Mercado, H., 1996. Dehydration of foods. Springer Science & Business Media. https://doi.org/10.1007/978-1-4757-2456-1.

Bonnet, J., Lenormand, R., 1997. Réalisation de micromodèles pour l'étude des écoulements polyphasiques en milieux poreux. Revue de l'. Insitut francais du petrole. 42, 477–480. https://doi.org/10.2516/ogst:1977026.

Cen, H., Lu, R., Mendoza, F., Beaudry, R.M., 2013. Relationship of the optical absorption and scattering properties with mechanical and structural properties of apple tissue. Postharvest Biol. Technol. 85, 30–38. https://doi.org/10.1016/j.postharvbio.2013.04.014.

Cortés, P., Badillo, G., Segura, L., Bouchon, P., 2014. Experimental evidence of water loss and oil uptake during simulated deep-fat frying using glass micromodels. J. Food Eng. 140, 19–27. https://doi.org/10.1016/j.jfoodeng.2014.04.005.

Cortés, P., Segura, L., Kawaji, M., Bouchon, P., 2015. The effect of gravity on moisture loss and oil absorption profiles during a simulated frying process using glass micromodels. Food Bioprod. Process. 95, 133–145. https://doi.org/10.1016/j.fbp.2015.05.001.

Cortés, P., Badillo, G., Segura, L., Bouchon, P., 2016. The effect of different porous media on moisture loss and oil absorption profiles during frying using glass micromodels. AIChE J. 62 (3), 629–638. https://doi.org/10.1002/aic.15088.

Daian, J.F., Saliba, J., 1991. Détermination d'un réseau aléatoire de pores pour modéliser la sorption et la migration d'humidité dans un mortier de ciment. Int. J. Heat Mass Transfer. 34 (8), 2081–2096. https://doi.org/10.1016/0017-9310(91)90219-5.

Defraeye, T., Radu, A., Derome, D., 2016. Recent advances in drying at interfaces of biomaterials. Drying Technol. 34 (16), 1904–1925. https://doi.org/10.1080/07373937.2016.1144062.

Díaz, R.E., Acuña, S.M., Segura, L.A., 2011. Construction of 2D transparent micromodels in polyester resin with porosity similar to carrots. Food Sci. Technol. 31 (4), 960–966. https://doi.org/10.1590/S0101-20612011000400022.

Duffy, D.C., McDonald, J.C., Schueller, O.J., Whitesides, G.M., 1998. Rapid prototyping of microfluidic systems in poly (dimethylsiloxane). Anal. Chem. 70 (23), 4974–4984. https://doi.org/10.1021/ac980656z.

Eloukabi, H., Sghaier, N., Prat, M., Ben Nassrallah, S., 2011. Drying experiments in a hydrophobic model porous medium in the presence of a dissolved salt. Chem. Eng. Technol. 34 (7), 1085–1094. https://doi.org/10.1002/ceat.201100064.

Fanta, S.W., Abera, M.K., Aregawi, W.A., Ho, Q.T., Verboven, P., Carmeliet, J., Nicolai, B.M., 2014. Microscale modeling of coupled water transport and mechanical deformation of fruit tissue during dehydration. J. Food Eng. 124, 86–96. https://doi.org/10.1016/j.jfoodeng.2013.10.007.

González-Fésler, M., Salvatori, D., Gómez, P., Alzamora, S.M., 2008. Convective air drying of apples as affected by blanching and calcium impregnation. J. Food Eng. 87 (3), 323–332. https://doi.org/10.1016/j.jfoodeng.2007.12.007.

Halder, A., Datta, A.K., Spanswick, R.M., 2011. Water transport in cellular tissues during thermal processing. AIChE J. 57 (9), 2574–2588. https://doi.org/10.1002/aic.12465.

Hallett, I.C., Macrae, E.A., Wegrzyn, T.F., 1992. Changes in kiwifruit cell wall ultrastructure and cell packing during postharvest ripening. Int. J. Plant Sci. 153 (1), 49–60. https://doi.org/10.1086/297006.

Herremans, E., Verboven, P., Verlinden, B.E., Cantre, D., Abera, M., Wevers, M., Nicolaï, B.M., 2015. Automatic analysis of the 3-D microstructure of fruit parenchyma tissue using X-ray micro-CT explains differences in aeration. BMC Plant Biol. 15 (1), 264. https://doi.org/10.1186/s12870-015-0650-y.

Huang, X., Qi, T., Wang, Z., Yang, D., Liu, X., 2012. A moisture transmembrane transfer model for pore network simulation of plant materials drying. Drying Technol. 30 (15), 1742–1749. https://doi.org/10.1080/07373937.2012.718306.

Jeffery, J., Holzenburg, A., King, S., 2012. Physical barriers to carotenoid bioaccessibility. Ultrastructure survey of chromoplast and cell wall morphology in nine carotenoid-containing fruits and vegetables. J. Sci. Food Agric. 92 (13), 2594–2602. https://doi.org/10.1002/jsfa.5767.

Joardder, M.U., Brown, R.J., Kumar, C., Karim, M.A., 2015. Effect of cell wall properties on porosity and shrinkage of dried apple. Int. J. Food Prop. 18 (10), 2327–2337. https://doi.org/10.1080/10942912.2014.980945.

Khan, M.I.H., Wellard, R.M., Nagy, S.A., Joardder, M.U.H., Karim, M.A., 2016. Investigation of bound and free water in plant-based food material using NMR T2 relaxometry. Innovative Food Sci. Emerging Technol. 38, 252–261. https://doi.org/10.1016/j.ifset.2016.10.015.

Khan, M.I.H., Wellard, R.M., Nagy, S.A., Joardder, M.U.H., Karim, M.A., 2017. Experimental investigation of bound and free water transport process during drying of hygroscopic food material. Int. J. Therm. Sci. 117, 266–273. https://doi.org/10.1016/j.ijthermalsci.2017.04.006.

Khan, M.I.H., Nagy, S.A., Karim, M.A., 2018a. Transport of cellular water during drying: An understanding of cell rupturing mechanism in apple tissue. Food Res. Int. 105, 772–781. https://doi.org/10.1016/j.foodres.2017.12.010.

Khan, M.I.H., Farrell, T., Nagy, S.A., Karim, M.A., 2018b. Fundamental understanding of cellular water transport process in bio-food material during drying. Sci. Rep. 8 (1), 15191. https://doi.org/10.1038/s41598-018-33159-7.

Laurindo, J.B., Prat, M., 1996. Numerical and experimental network study of evaporation in capillary porous media. Phase distributions. Chem. Eng. Sci. 51 (23), 5171–5185. https://doi.org/10.1016/S0009-2509(96)00341-7.

Laurindo, J.B., Prat, M., 1998. Numerical and experimental network study of evaporation in capillary porous media. Drying rates. Chem. Eng. Sci. 53 (12), 2257–2269. https://doi.org/10.1016/S0009-2509(97)00348-5.

Lewicki, P.P., 2006. Design of hot air drying for better foods. Trends Food Sci. Technol. 17 (4), 153–163. https://doi.org/10.1016/j.tifs.2005.10.012.

Metzger, T., Irawan, A., Tsotsas, E., 2007. Influence of pore structure on drying kinetics: A pore network study. AIChE J. 53 (12), 3029–3041. https://doi.org/10.1002/aic.11307.

Mujumdar, A.S., 2006. Handbook of Industrial Drying. CRC Press, Boca Raton. Doi: 10.1201/9781420017618.

Nowicki, S.C., Davis, H.T., Scriven, L.E., 1992. Microscopic determination of transport paraheters in drying porous media. Drying Technol. 10 (4), 925–946. https://doi.org/10.1080/07373939208916488.

Oyarzún, C.A., Segura, L.A., 2009. Design and construction of glass micromodels for the study of moisture transport in softwoods. Drying Technol. 27 (1), 14–29. https://doi.org/10.1080/07373930802565731.

Pieczywek, P.M., Zdunek, A., 2012. Automatic classification of cells and intercellular spaces of apple tissue. Comp. Electron. Agric. 81, 72–78. https://doi.org/10.1016/j.compag.2011.11.006.

Prat, M., 1993. Percolation model of drying under isothermal conditions in porous media. Int. J. Multiphase Flow. 19 (4), 691–704. https://doi.org/10.1016/0301-9322(93)90096-D.

Rahman, M.M., Kumar, C., Joardder, M.U., Karim, M.A., 2018a. A micro-level transport model for plant-based food materials during drying. Chem. Eng. Sci. 187, 1–15. https://doi.org/10.1016/j.ces.2018.04.060.

Rahman, M.M., Joardder, M.U., Karim, A., 2018b. Non-destructive investigation of cellular level moisture distribution and morphological changes during drying of a plant-based food material. Biosyst. Eng. 169, 126–138. https://doi.org/10.1016/j.ces.2018.04.060.

Ramírez, C., Troncoso, E., Muñoz, J., Aguilera, J.M., 2011. Microstructure analysis on pre-treated apple slices and its effect on water release during air drying. J. Food Eng. 106 (3), 253–261. https://doi.org/10.1016/j.jfoodeng.2011.05.020.

Roy, S., Watada, A.E., Wergin, W.P., 1997. Characterization of the cell wall microdomain surrounding plasmodesmata in apple fruit. Plant Physiol. 114 (2), 539–547. https://doi.org/10.1104/pp.114.2.539.

SanMartin, F.A., Laurindo, J.B., Segura, L.A., 2011. Pore-scale simulation of drying of a porous media saturated with a sucrose solution. Drying Technol. 29 (8), 873–887. https://doi.org/10.1080/07373937.2010.547968.

Segura, L.A., Toledo, P.G., 2005. Pore-level modeling of isothermal drying of pore networks: Effects of gravity and pore shape and size distributions on saturation and transport parameters. Chem. Eng. J. 111 (2–3), 237–252. https://doi.org/10.1016/j.cej.2005.02.004.

Segura, L.A., 2007. Modeling at pore-scale isothermal drying of porous materials: Liquid and vapor diffusivity. Drying Technol. 25 (10), 1677–1686. https://doi.org/10.1080/07373930701590889.

Segura, L.A., Oyarzún, C.A., 2012. Experimental evidence of mass transfer mechanisms during freeze-drying in a capillary porous medium. Int. J. Refrigeration 35 (8), 2102–2109. https://doi.org/10.1016/j.ijrefrig.2012.08.014.

Segura, L.A., Badillo, G.M., Villagra, F.V., Garrido, D.L., 2013. Protocol to build 2D Transparent PDMS micromodels for use in drying experiments. In: Proceedings of the 6th Nordic Drying Conference (NDC 2013), Danish Technological Institute and NTNU Trondheim (Norwegian University of Science and Technology), Danish Technological Institute, Copenhagen. 11 pages.

Segura, L., Fuentes, M., Urrutia, C., Badillo, G., 2015. 3D PDMS transparent micromodels simulating a food matrix: micromodel fabrication protocol and preliminary drying experiments. Blucher Chem. Eng. Proc. 1 (2), 2942–2949. https://doi.org/10.5151/chemeng-cobeq2014-0006-27656-154433.

Sghaier, N., Prat, M., 2009. Effect of efflorescence formation on drying kinetics of porous media. Trans. Porous Med. 80 (3), 441. https://doi.org/10.1007/s11242-009-9373-6.

Shaw, T.M., 1986. Movement of a drying front in a porous material. MRS Online Proceedings Library Archive 73. https://doi.org/10.1557/PROC-73-215.

Shaw, T.M., 1987. Drying as an immiscible displacement process with fluid counterflow. Phys. Rev. Lett. 59 (15), 1671. https://doi.org/10.1103/PhysRevLett. 59.1671.

Sutherland, P., Hallett, I., Redgwell, R., Benhamou, N., MacRae, E., 1999. Localization of cell wall polysaccharides during kiwifruit (Actinidia deliciosa) ripening. Int. J. Plant Sci. 160 (6), 1099–1109. https://doi.org/10.1086/314196.

Varela, P., Salvador, A., Fiszman, S., 2007. Changes in apple tissue with storage time: Rheological, textural and microstructural analyses. J. Food Eng. 78 (2), 622–629. https://doi.org/10.1016/j.jfoodeng.2005.10.034.

Vicent, V., Verboven, P., Ndoye, F.T., Alvarez, G., Nicolaï, B., 2017. A new method developed to characterize the 3D microstructure of frozen apple using X-ray micro-CT. J. Food Eng. 212, 154–164. https://doi.org/10.1016/j.jfoodeng.2017.05.028.

Vorhauer, N., Tran, Q.T., Metzger, T., Tsotsas, E., Prat, M., 2013. Experimental investigation of drying in a model porous medium: Influence of thermal gradients. Drying Technol. 31 (8), 920–929. https://doi.org/10.1080/07373937.2012.724750.

Xiao, B., Chang, J., Huang, X., Liu, X., 2014. A moisture transfer model for isothermal drying of plant cellular materials based on the pore network approach. Drying Technol. 32 (9), 1071–1081. https://doi.org/10.1080/07373937.2014.883629.